Saarakkala, Seppo E.; Sokolov, Maksim; Hinkkanen, Marko; Kataja, Jari; Tammi, Kari

# State-space flux-linkage control of bearingless synchronous reluctance motors

*Published in:*
IEEE Energy Conversion Congress and Exposition (ECCE 2016)

*DOI:*
10.1109/ECCE.2016.7855464

Published: 18/09/2016

*Document Version*
Peer-reviewed accepted author manuscript, also known as Final accepted manuscript or Post-print

*Please cite the original version:*
Saarakkala, S. E., Sokolov, M., Hinkkanen, M., Kataja, J., & Tammi, K. (2016). State-space flux-linkage control of bearingless synchronous reluctance motors. In *IEEE Energy Conversion Congress and Exposition (ECCE 2016)* (IEEE Energy Conversion Congress & Exposition). IEEE. https://doi.org/10.1109/ECCE.2016.7855464

# State-Space Flux-Linkage Control of Bearingless Synchronous Reluctance Motors

Seppo E. Saarakkala*, Maksim Sokolov*, Marko Hinkkanen*, Jari Kataja†, and Kari Tammi§
*Aalto University School of Electrical Engineering, P.O. Box 13000, FI-00076 Aalto, Finland
†VTT Technical Research Centre of Finland, Finland
§Aalto University School of Engineering, Finland

***Abstract*—This paper deals with a model-based state-space flux-linkage control of a dual three-phase-winding bearingless synchronous reluctance motor. Analytical tuning rules for the state feedback, integral action, and reference feedforward gains are derived in the continuous-time domain. The proposed method is easy to apply: the desired closed-loop bandwidth together with the estimated magnetic-model of the motor are required. Furthermore, the proposed method automatically takes into account the mutual coupling between the two windings. A simple digital implementation is provided and the robustness of the proposed control method against the system parameter inaccuracies and eccentric rotor positions is analyzed. The proposed controller design is evaluated by means of simulations by keeping in mind the most important aspects related to an experimental evaluation.**

## I. Introduction

In recent years, bearingless machines have received increasing attention as an alternative to conventional mechanical bearings or active-magnetic-bearings (AMBs), especially in high-speed applications [1]. Bearingless drives incorporate the functions of active magnetic bearings and electrical machine in one unit, which reduces the size, complexity and price of the system [2]. Several motor topologies have been proposed in the literature to be used as bearingless motors, e.g., [2]–[5]. Particularly in lower speed and higher power applications, a bearingless synchronous reluctance motor (BSyRM) is an attractive alternative. The advantages of BSyRM are, e.g., that it neither needs the permanent magnets (PMs) placed in the rotor, like the PM machines do, nor it produces additional losses because of the rotor currents, like the induction machines do. However, the synchronous reluctance motors are often operated with relatively high currents, which means that the magnetic circuit of the motor is saturated.

The BSyRM considered in this paper includes two separate sets of three-phase windings. The first winding set is for production of the shaft torque and is referred to as a main winding. The second winding set is for production of the radial force for stable levitation of the rotor and is referred to as a suspension winding. For independent and rapid production of the required torque and force, the performance of the inner flux-linkage (or current) control loop is especially important since it has a direct influence on the overall stability of the system. Moreover, the inner control loop sets the dynamic limitations for the outer control loops, i.e., the speed-control loop and the radial-position control loop.

Unbalanced vibration frequency in high-speed applications can be quite large, as it is proportional to rotation speed. The control loop has to have sufficient bandwidth in order to compensate for such unbalance in rigid rotors [6]. Also, the bending modes of the rotor have to be taken into account in high-speed applications. Typically, the first vibration modes that need to be controlled occur at frequencies under 1000 Hz [7]–[9]. Hence, the control system has to be able to reach a bandwidth close to 1 kHz to be applicable in areas demanding high-speed operation – up to rotational speeds of 60 kr/min. Another requirement is to reach the specified performance without excess increase in switching frequency. That would allow a simpler implementation by using commercially available inverters.

Two major factors to be taken into account when designing the flux-linkage (or current) control loop for bearingless motors are that the electrical parameters of the system change due to the radial displacement of the rotor and due to the magnetic-saturation state of the motor [10]. These phenomena may limit the applicability of conventional current-control design methods [11]–[13] and require more sophisticated ways of approaching the problem. In some cases, the effects of coupling are reasonably small and do not cause instability, hence they can be omitted as in [14] and [15]. Several papers present different decoupling methods, e.g., [10], [16]. However, none of the papers present analytical tuning rules for the current controllers, which makes it difficult to apply these methods to different machines.

In this paper, a model-based analytical design method for a state-space flux-linkage control of BSyRMs is proposed. The main contributions of this paper are:

1) Simple analytical design rules of the state-space flux-linkage controller (including both the feedback and feedforward gains) are presented.
2) Robustness against the system parameter inaccuracies and eccentric rotor positions is analyzed.

According to the authors' knowledge, analytical design rules for neither the flux-linkage controller nor the current controller for BSyRMs have been proposed before.

## II. System Model

As depicted in Fig. 1(a), the studied BSyRM has a 4-pole multi-flux-barrier rotor. A 4-pole main winding for the torque production and a 2-pole suspension winding for the radial-force production are sinusoidally distributed in the stator. In the following, the system model is analyzed in synchronous coordinates, rotating at twice the speed of the shaft $\omega_{\mathrm{M}}$.

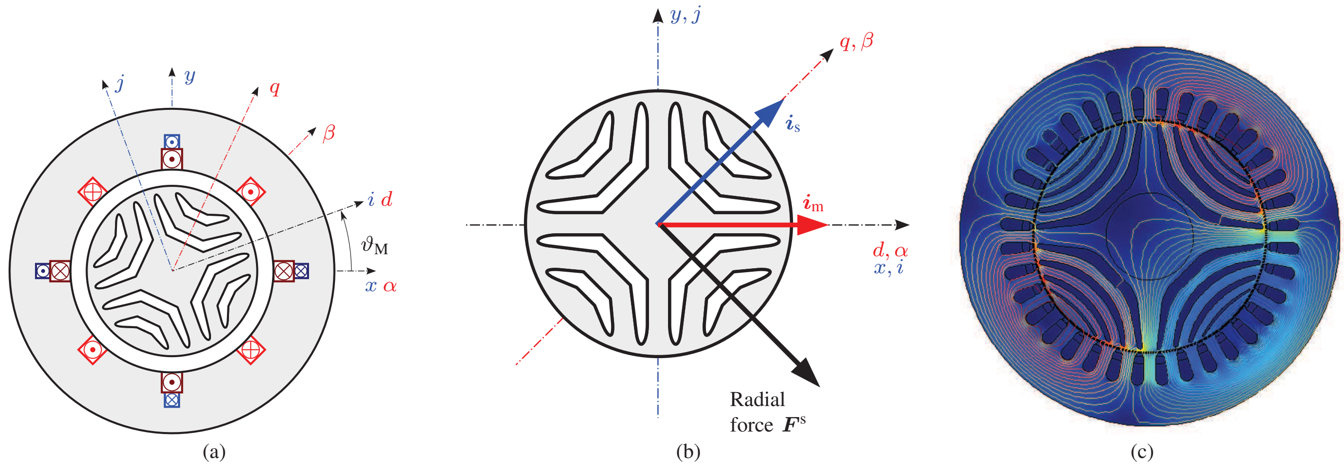


Fig. 1. The BSyRM studied in this paper: (a) Coordinate systems required for the flux-linkage controller. The stationary coordinates of the main and suspension windings are marked with ($\alpha$, $\beta$) and ($x$, $y$), respectively. Similarly, the rotating coordinates of the main and suspension windings are marked with ($d$, $q$) and ($i$, $j$), respectively; (b) Current vectors $\boldsymbol{i}_\mathrm{m}$ and $\boldsymbol{i}_\mathrm{s}$ together with radial-force vector for one operating point; and (c) The corresponding magnetic-field solution computed with FE software.

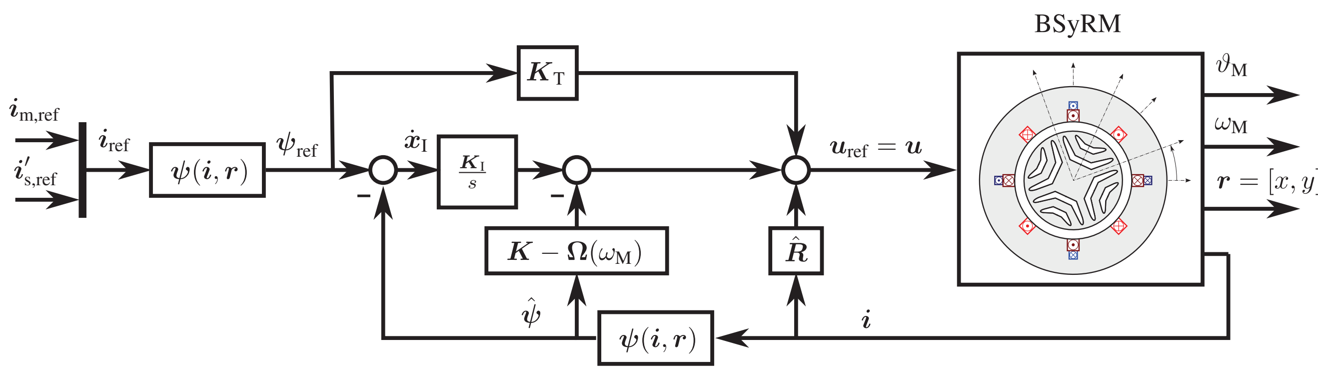


Fig. 2. State-space flux-linkage control structure. The controller consists of a state feedback, an integral action, and a reference feedforward. For simplicity, the block diagram is shown in synchronous coordinates, i.e., coordinate transformations are not depicted.

TABLE I
EXPLICIT-FUNCTION COEFFICIENTS

| Parameter | $L_{\mathrm{q},0}$ [mH] | $a$ [mH] | $b$ [1/A$^2$] | $L_{\mathrm{s},0}$ [mH] | $c$ [mH/A$^2$] | $d$ [1/A$^2$] | $M_{\mathrm{d},0}$ [H/m] | $e$ $\left[\frac{\mathrm{H}}{\mathrm{m}\cdot\mathrm{A}^2}\right]$ | $f$ [1/A$^2$] |
|---|---|---|---|---|---|---|---|---|---|
| Value | 2.7 | 6 | 0.006 | 37.3 | 1.3 | 0.07 | 31.28 | 0.18 | 0.026 |

### A. Voltage Equations and Flux-Linkage Equations

The voltage equations of the main winding (marked with subscript m) and the suspension winding (marked with subscript s) can be given as a combined state-space representation [2]

$$\frac{\mathrm{d}}{\mathrm{d}t}\begin{bmatrix}\boldsymbol{\psi}_\mathrm{m}\\ \boldsymbol{\psi}_\mathrm{s}\end{bmatrix} = \begin{bmatrix}\boldsymbol{u}_\mathrm{m}\\ \boldsymbol{u}_\mathrm{s}\end{bmatrix} - \begin{bmatrix}R_\mathrm{m}\boldsymbol{I} & \boldsymbol{0}\\ \boldsymbol{0} & R_\mathrm{s}\boldsymbol{I}\end{bmatrix}\boldsymbol{i} - \begin{bmatrix}2\omega_\mathrm{M}\boldsymbol{J} & \boldsymbol{0}\\ \boldsymbol{0} & \omega_\mathrm{M}\boldsymbol{J}\end{bmatrix}\begin{bmatrix}\boldsymbol{\psi}_\mathrm{m}\\ \boldsymbol{\psi}_\mathrm{s}\end{bmatrix} \tag{1}$$

where $\boldsymbol{J} = \left[\begin{smallmatrix}0 & -1\\ 1 & 0\end{smallmatrix}\right]$, $\boldsymbol{I}$ is a $2\times 2$ identity matrix and $\boldsymbol{0}$ is a $2\times 2$ null matrix. The voltage vectors are defined as $\boldsymbol{u}_\mathrm{m} = \begin{bmatrix}u_\mathrm{md} & u_\mathrm{mq}\end{bmatrix}^\mathrm{T}$ and $\boldsymbol{u}_\mathrm{s} = \begin{bmatrix}u_\mathrm{sd} & u_\mathrm{sq}\end{bmatrix}^\mathrm{T}$. The current vectors and the flux-linkage vectors are defined similarly. The resistances of the windings are $R_\mathrm{m}$ and $R_\mathrm{s}$, respectively. The angular speed of the shaft is defined as $\omega_\mathrm{M} = \mathrm{d}\vartheta_\mathrm{M}/\mathrm{d}t$, where $\vartheta_\mathrm{M}$ is the angular position of the shaft.

With linear magnetics, the flux linkages of the main winding $\boldsymbol{\psi}_\mathrm{m}$ and the suspension winding $\boldsymbol{\psi}_\mathrm{s}$ can be presented in matrix format [2]:

$$\begin{bmatrix}\boldsymbol{\psi}_\mathrm{m}\\ \boldsymbol{\psi}_\mathrm{s}\end{bmatrix} = \underbrace{\begin{bmatrix}\boldsymbol{L}_\mathrm{m} & \boldsymbol{M}\\ \boldsymbol{M}^\mathrm{T} & \boldsymbol{L}_\mathrm{s}\end{bmatrix}}_{\boldsymbol{L}_\Sigma}\begin{bmatrix}\boldsymbol{i}_\mathrm{m}\\ \boldsymbol{i}_\mathrm{s}\end{bmatrix} \qquad \boldsymbol{L}_\mathrm{m} = \begin{bmatrix}L_\mathrm{d} & 0\\ 0 & L_\mathrm{q}\end{bmatrix}, \tag{2}$$

$$\boldsymbol{L}_\mathrm{s} = \begin{bmatrix}L_\mathrm{s} & 0\\ 0 & L_\mathrm{s}\end{bmatrix}, \qquad \boldsymbol{M} = \begin{bmatrix}M'_\mathrm{d}i & -M'_\mathrm{d}j\\ M'_\mathrm{q}j & M'_\mathrm{q}i\end{bmatrix}$$

where $L_\mathrm{d}$, $L_\mathrm{q}$, $L_\mathrm{s}$ are inductances and $M'_\mathrm{d}$, $M'_\mathrm{q}$ are radial-force constants. The rotor displacements are denoted as $i$ and $j$, cf. Fig. 1(a). It can be noted that the cross coupling between the main winding and the suspension winding exists only when $i$ and $j$ are nonzero, i.e., when the rotor is not centric.

### B. Explicit-Function Based Magnetic Model

It has been demonstrated in several studies, that it is unrealistic to assume a linear magnetic circuit in SyRMs and BSyRMs [10], [17]. Thus, instead of using (2), the flux linkages are modeled as functions of currents in [18]. The calculation is based on static finite-element analysis (FEA) in 9000 pre-selected operating points. As an example, Fig. 1(b) shows the pre-defined current vectors $\boldsymbol{i}_\mathrm{m}$ and $\boldsymbol{i}_\mathrm{s}$ for one operating point and Fig. 1(c) shows the corresponding magnetic-field solution. Based on the FEA results, the following explicit-function based magnetic model was used in [18] to obtain the system-parameter estimates

$$\hat{\psi}_\mathrm{md}(i_\mathrm{md}) = \hat{L}_\mathrm{d} i_\mathrm{md}, \qquad \hat{\psi}_\mathrm{mq}(i_\mathrm{mq}) = \hat{L}_\mathrm{q}(i_\mathrm{mq}) i_\mathrm{mq} \tag{3}$$

$$\hat{\psi}_\mathrm{sd}(i_\mathrm{mq}, i_\mathrm{sd}) = \hat{L}_\mathrm{s}(i_\mathrm{mq}) i_\mathrm{sd}, \qquad \hat{\psi}_\mathrm{sq}(i_\mathrm{mq}, i_\mathrm{sq}) = \hat{L}_\mathrm{s}(i_\mathrm{mq}) i_\mathrm{sq}$$

$$\hat{L}_\mathrm{q}(i_\mathrm{mq}) = L_\mathrm{q,0} + \frac{a}{1 + b i_\mathrm{mq}^2}, \qquad \hat{L}_\mathrm{s}(i_\mathrm{mq}) = L_\mathrm{s,0} - \frac{c i_\mathrm{mq}^2}{1 + d i_\mathrm{mq}^2}$$

$$\hat{M}'_\mathrm{d}(i_\mathrm{mq}) = M_\mathrm{d,0} - \frac{e i_\mathrm{mq}^2}{1 + f i_\mathrm{mq}^2} \tag{4}$$

where $L_\mathrm{q,0}$, $L_\mathrm{s,0}$, $a$, $b$, $c$, $d$, $e$, and $f$ are the coefficients of the inductance functions. The numerical values of the magnetic model are given in Table I. The constant parameters are estimated as $\hat{L}_\mathrm{d} = 15$ mH and $\hat{M}'_\mathrm{q} = 0.66$ H/m. By substituting these inductance estimates into (2), then the inductance-matrix estimate $\hat{\boldsymbol{L}}_\Sigma$ is obtained and it is applied in the flux-linkage controller.

## III. Flux-Linkage Controller Design Based on Internal-Model Control (IMC) Principle

Fig. 2 shows the proposed flux-linkage controller structure. It is worth keeping in mind that $\boldsymbol{u}_\mathrm{s}$, $\boldsymbol{i}_\mathrm{s}$, and $\boldsymbol{\psi}_\mathrm{s}$ in (1) are varying sinusoidally, with the angular frequency $\omega_\mathrm{M}$, when the motor shaft is rotating and the radial force is produced. Thus, the electrical-angular frequencies of both windings are the same. In order to control the torque and the radial force without steady-state errors, the flux linkages of both windings are controlled in synchronous-coordinate system (rotating at the electrical-angular frequency of $2\omega_\mathrm{M}$). The voltage equations are defined in this coordinate system as

$$\frac{\mathrm{d}\boldsymbol{\psi}}{\mathrm{d}t} = \boldsymbol{u} - \boldsymbol{R}\boldsymbol{i} - \boldsymbol{\Omega}(\omega_\mathrm{M})\boldsymbol{\psi} \tag{5}$$

where

$$\boldsymbol{R} = \begin{bmatrix} R_\mathrm{m}\boldsymbol{I} & \boldsymbol{0} \\ \boldsymbol{0} & R_\mathrm{s}\boldsymbol{I} \end{bmatrix} \qquad \boldsymbol{\Omega}(\omega_\mathrm{M}) = \begin{bmatrix} 2\omega_\mathrm{M}\boldsymbol{J} & \boldsymbol{0} \\ \boldsymbol{0} & 2\omega_\mathrm{M}\boldsymbol{J} \end{bmatrix}$$

Furthermore, the mutual-coupling matrix $\boldsymbol{M}$ is defined as

$$\boldsymbol{M}' = \begin{bmatrix} M'_\mathrm{d} x & -M'_\mathrm{d} y \\ M'_\mathrm{q} y & M'_\mathrm{q} x \end{bmatrix} \tag{6}$$

An ideal voltage source is assumed when designing the controller, i.e., $\boldsymbol{u} = \boldsymbol{u}_\mathrm{ref}$. Moreover, because the current vector is a measured output of the system and the relation between the flux linkages and the currents is known (cf. Section II-B), both $\boldsymbol{i}$ and $\boldsymbol{\psi}$ are available for the control. In the IMC principle [11], the open-loop dynamics of the system is first cancelled by using appropriate feedback compensations. Then, the feedback controller together with the feedforward compensator are designed to obtain the desired dynamics for the closed-loop system.

### A. State-Feedback Control with Integral Action and Reference Feedforward

The control law is given as

$$\boldsymbol{u}_\mathrm{ref} = -[\boldsymbol{K} - \boldsymbol{\Omega}(\omega_\mathrm{M})]\hat{\boldsymbol{\psi}} + \hat{\boldsymbol{R}}\boldsymbol{i} + \boldsymbol{K}_\mathrm{I}\boldsymbol{x}_\mathrm{I} + \boldsymbol{K}_\mathrm{T}\boldsymbol{\psi}_\mathrm{ref} \tag{7}$$

where $\boldsymbol{K}$, $\boldsymbol{K}_\mathrm{I}$, and $\boldsymbol{K}_\mathrm{T}$ are the controller matrices. The integral state is defined as

$$\frac{\mathrm{d}\boldsymbol{x}_\mathrm{I}}{\mathrm{d}t} = \boldsymbol{\psi}_\mathrm{ref} - \hat{\boldsymbol{\psi}} \tag{8}$$

When (7) is substituted into (5), the closed-loop system is

$$\frac{\mathrm{d}\boldsymbol{\psi}}{\mathrm{d}t} = -\boldsymbol{K}\hat{\boldsymbol{\psi}} + \boldsymbol{K}_\mathrm{I}\boldsymbol{x}_\mathrm{I} + \boldsymbol{K}_\mathrm{T}\boldsymbol{\psi}_\mathrm{ref} + \boldsymbol{\Omega}(t)(\hat{\boldsymbol{\psi}} - \boldsymbol{\psi}) + (\hat{\boldsymbol{R}} - \boldsymbol{R})\boldsymbol{i} \tag{9}$$

With accurate parameter estimates and mechanical-state measurements $\boldsymbol{\psi} = \hat{\boldsymbol{\psi}}$ and $\boldsymbol{R} = \hat{\boldsymbol{R}}$, and thus, the closed-loop system reduces to $d\boldsymbol{\psi}/dt = -\boldsymbol{K}\boldsymbol{\psi} + \boldsymbol{K}_\mathrm{I}\boldsymbol{x}_\mathrm{I} + \boldsymbol{K}_\mathrm{T}\boldsymbol{\psi}_\mathrm{ref}$. The closed-loop system equation can be presented in the Laplace domain as:

$$s\boldsymbol{I}_4\boldsymbol{\psi} = -\boldsymbol{K}\boldsymbol{\psi} + \boldsymbol{K}_\mathrm{I}\left(\frac{\boldsymbol{\psi}_\mathrm{ref}}{s} - \frac{\boldsymbol{\psi}}{s}\right) + \boldsymbol{K}_\mathrm{T}\boldsymbol{\psi}_\mathrm{ref} \tag{10}$$

where $\boldsymbol{I}_4$ is a $4 \times 4$ identity matrix and $s$ is the Laplace operator. The closed-loop transfer-function matrix from $\boldsymbol{\psi}_\mathrm{ref}$ to $\boldsymbol{\psi}$ is

$$\boldsymbol{G}_\mathrm{c}(s) = (s^2\boldsymbol{I}_4 + \boldsymbol{K}s + \boldsymbol{K}_\mathrm{I})^{-1}(\boldsymbol{K}_\mathrm{T}s + \boldsymbol{K}_\mathrm{I}) \tag{11}$$

If diagonal control matrices are selected, the closed-loop dynamics of each state variable are decoupled. If a first-order closed-loop system is selected for each of the system states, then the desired closed-loop transfer-function matrix is

$$\boldsymbol{G}_\mathrm{c*}(s) = \frac{\alpha_\mathrm{c}}{s + \alpha_\mathrm{c}}\boldsymbol{I}_4 \tag{12}$$

where $\alpha_\mathrm{c}$ is the closed-loop system bandwidth. By selecting the controller matrices in (11) as

$$\boldsymbol{K} = 2\alpha_\mathrm{c}\boldsymbol{I}_4, \qquad \boldsymbol{K}_\mathrm{I} = \alpha_\mathrm{c}^2\boldsymbol{I}_4, \qquad \boldsymbol{K}_\mathrm{T} = \alpha_\mathrm{c}\boldsymbol{I}_4 \tag{13}$$

then (11) equals (12).

It is worth mentioning that the IMC principle is not the only possible approach for the controller design. Other approaches, such as the complex vector design for PM machines [12], [13], could be applied as well. Furthermore, by changing (12), different closed-loop dynamics could be easily selected. As an example, different closed-loop system bandwidths could be selected for the main and suspension windings.

### B. Reference Calculation

The torque of the motor can be defined as [10]

$$T_\mathrm{e} = 3(L_\mathrm{d} - L_\mathrm{q}) i_\mathrm{md} i_\mathrm{mq} \tag{14}$$

When the motor-torque reference $T_\mathrm{e,ref}$ is known, then the current references $i_\mathrm{md,ref}$ and $i_\mathrm{mq,ref}$ can be solved from (14), e.g., by applying the maximum-torque-per-ampere (MTPA) principle. Alternatively, the motor may be operated with constant magnetization state, i.e., constant $i_\mathrm{md,ref}$ is first selected and $i_\mathrm{mq,ref}$ is then calculated from (14). Moreover, when the reference-force vector in xy coordinates $\boldsymbol{F}_\mathrm{ref}^\mathrm{s}$ is known, then

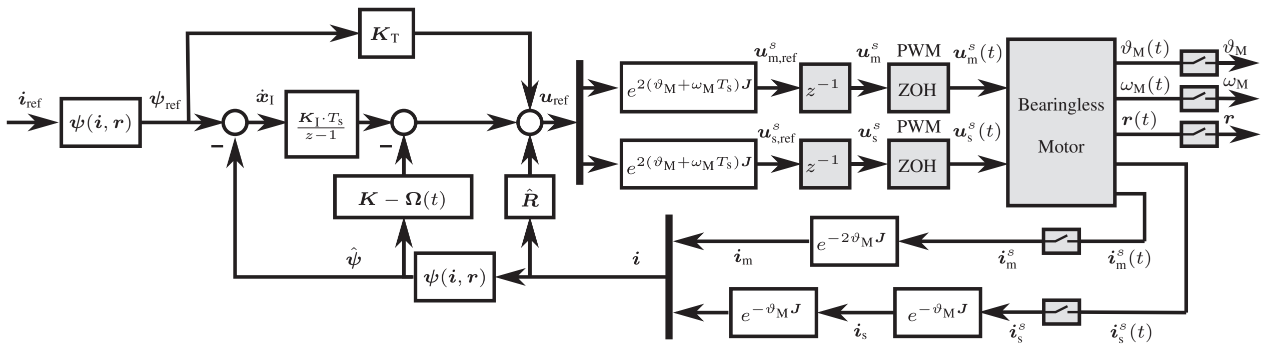

Fig. 3. Discrete-time implementation of the proposed flux-linkage controller. The gray blocks represent the physical system (including the bearingless motor, PWMs, samplers, and inherent computational delays $z^{-1}$). The bearingless motor block consists of (16) and the coordinate transformations. The angular error due to the time delay is compensated for in the coordinate transformation of the stator voltage.

the suspension winding current-reference vector $\boldsymbol{i}'_{\text{s,ref}}$ can be solved from [10]

$$\boldsymbol{F}^{\text{s}}_{\text{ref}} = \begin{bmatrix} F_{\text{x}} \\ F_{\text{y}} \end{bmatrix} = \begin{bmatrix} M'_{\text{d}} i_{\text{md}} & M'_{\text{q}} i_{\text{mq}} \\ M'_{\text{q}} i_{\text{mq}} & -M'_{\text{d}} i_{\text{md}} \end{bmatrix} \boldsymbol{i}'_{\text{s,ref}} \tag{15}$$

In the following simulations, the motor is operated in the torque-control mode (i.e., the torque reference is manually defined). The suspension winding is operated in the force-control mode, meaning that the reference-force vector is manually defined.

## IV. Discrete-Time Implementation

Fig. 3 presents a discrete-time implementation of the proposed flux-linkage controlled BSyRM. It consists of the continuous-time BSyRM plant model, the flux-linkage controller (with the integral state discretized by the forward Euler approximation), pulsewidth modulators (PWMs), and samplers. Sampling is assumed to be synchronized with the PWM and two samples per switching period are taken, meaning that the sampling time $T_{\text{s}} = 1/(2f_{\text{sw}})$, where $f_{\text{sw}}$ is the switching frequency. The switching cycle averaged quantities are considered. Hence, the actual stator voltages $\boldsymbol{u}^s_{\text{m}}$ and $\boldsymbol{u}^s_{\text{s}}$ in stator coordinates are piecewise constant between two consecutive sampling instants, which corresponds to the ZOH in stator coordinates.

When the system parameters are known, the closed-loop system bandwidth $\alpha_{\text{c}}$ and the switching frequency are the remaining parameters to be selected by the control designer. These parameters are selected based on the stability analysis of the closed-loop system. Moreover, the robustness of the proposed control method against the system parameter inaccuracies and eccentric rotor positions is analyzed.

### A. Closed-Loop System Stability

By combining (2), (5) and (6), the continuous-time state-space representation can be obtained

$$\begin{aligned} \frac{\mathrm{d}\boldsymbol{\psi}(t)}{\mathrm{d}t} &= \boldsymbol{A}(t)\boldsymbol{\psi}(t) + \boldsymbol{B}\boldsymbol{u}(t) \\ \boldsymbol{i}(t) &= \boldsymbol{L}_{\Sigma}^{-1}\boldsymbol{\psi}(t) \end{aligned} \tag{16}$$

where

$$\boldsymbol{A}(t) = -\boldsymbol{R}\boldsymbol{L}_{\Sigma}^{-1} - \boldsymbol{\Omega}(\omega_{\text{M}}), \quad \boldsymbol{B} = \boldsymbol{I}_4$$

When the ZOH is modelled in stator coordinates, the discrete-time plant model, corresponding to (16), is

$$\begin{aligned} \boldsymbol{\psi}(k+1) &= \boldsymbol{\Phi}\boldsymbol{\psi}(k) + \boldsymbol{\Gamma}\boldsymbol{u}(k) \\ \boldsymbol{i}(k) &= \boldsymbol{L}_{\Sigma}^{-1}\boldsymbol{\psi}(k) \end{aligned} \tag{17}$$

where the system matrices are

$$\boldsymbol{\Phi} = e^{\boldsymbol{A}T_{\text{s}}}, \quad \boldsymbol{\Gamma} = \int_0^{T_{\text{s}}} e^{\boldsymbol{A}\tau} \begin{bmatrix} e^{-2\omega_{\text{M}}(T_{\text{s}}-\tau)\boldsymbol{J}} & \boldsymbol{0} \\ \boldsymbol{0} & e^{-2\omega_{\text{M}}(T_{\text{s}}-\tau)\boldsymbol{J}} \end{bmatrix} \mathrm{d}\tau$$

These matrices can be solved either numerically or by finding closed-form expressions for the matrix elements. In this work, the matrices are used only for the stability analysis, and thus, solved numerically.

When the discrete-time plant model (17) is applied together with the discretized flux-linkage controller (cf. Fig. 3), then the closed-loop system matrix becomes

$$\begin{bmatrix} \boldsymbol{\psi}(k+1) \\ \boldsymbol{u}(k+1) \\ \boldsymbol{x}_{\text{I}}(k+1) \end{bmatrix} = \tag{18}$$
$$\underbrace{\begin{bmatrix} \boldsymbol{\Phi} & \boldsymbol{\Gamma} & \boldsymbol{0}_4 \\ \hat{\boldsymbol{R}}\boldsymbol{L}_{\Sigma}^{-1} - [\boldsymbol{K} - \boldsymbol{\Omega}(\omega_{\text{M}})]\hat{\boldsymbol{L}}_{\Sigma}\boldsymbol{L}_{\Sigma}^{-1} & \boldsymbol{0}_4 & \boldsymbol{K}_{\text{I}} \\ -T_{\text{s}}\hat{\boldsymbol{L}}_{\Sigma}\boldsymbol{L}_{\Sigma}^{-1} & \boldsymbol{0}_4 & \boldsymbol{I}_4 \end{bmatrix}}_{\boldsymbol{\Phi}_{\text{cl}}} \begin{bmatrix} \boldsymbol{\psi}(k) \\ \boldsymbol{u}(k) \\ \boldsymbol{x}_{\text{I}}(k) \end{bmatrix}$$

where $\boldsymbol{0}_4$ is $4 \times 4$ null matrix. The stability of the closed-loop system is defined by the eigenvalues of $\boldsymbol{\Phi}_{\text{cl}}$ in (18). If all the eigenvalues are inside the unit circle, the system is stable. Otherwise the closed-loop system is unstable.

At first, the selection of the switching frequency [$f_{\text{sw}} = 1/(2T_{\text{s}})$] and the flux-linkage control-loop bandwidth is analyzed by examining the stability of the closed-loop system. Accurate system-parameter estimates are assumed, i.e., $\hat{\boldsymbol{L}}_{\Sigma} = \boldsymbol{L}_{\Sigma}$ and $\hat{\boldsymbol{R}} = \boldsymbol{R}$. The rotor is assumed to be centric (i.e., $x = y = 0$) and it rotates 1500 r/min. The switching frequency is varied between $4 \ldots 16$ kHz, which are typical values for commercial frequency converters. The flux-linkage control-loop bandwidth is varied between $200 \ldots 1000$ Hz. The white region in Fig. 4 represents stable parameter combinations and the cyan-shaded region represents unstable parameter combinations. As an example, the parameter selection of $f_{\text{sw}} = 8$ kHz and $\alpha_{\text{c}} = 2\pi \cdot 600$ rad/s (marked with red cross in Fig. 4)

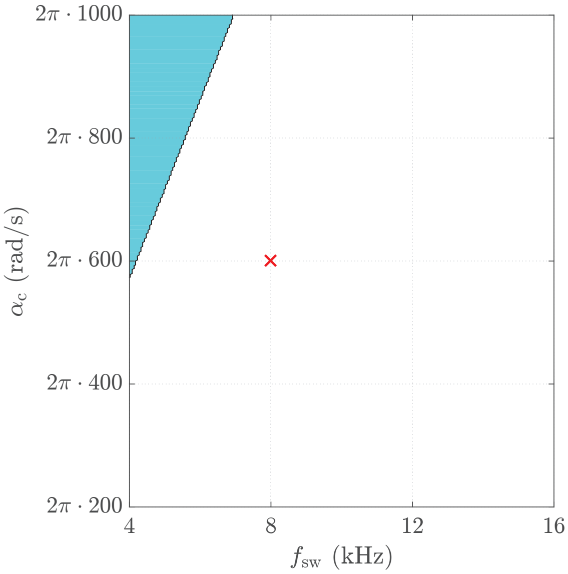


Fig. 4. Stability regions, when $\alpha_c$ and $f_{sw} = 1/(2T_s)$ are varied. The white area represents a stable system, whilst the cyan-shaded area represents an unstable system. The red cross indicates one feasible parameter combination, which will be used in this paper.

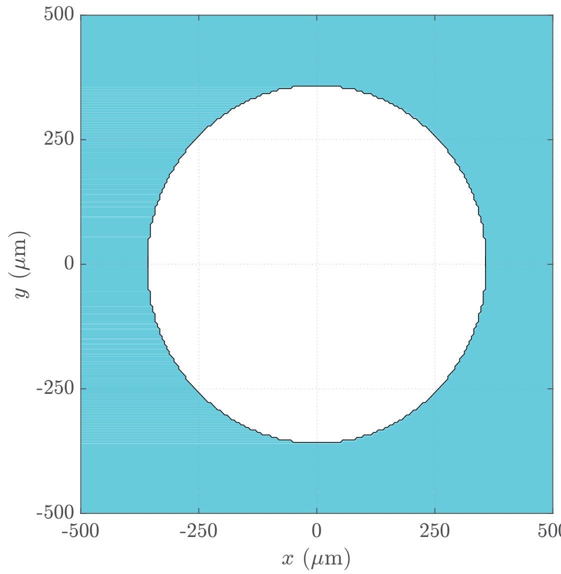


Fig. 6. Stability regions, when the rotor displacements are varied in the plant model (6). The mutual coupling between the windings is neglected in the controller, i.e., $\hat{\boldsymbol{M}}' = \boldsymbol{0}$. The white area presents a stable system, whilst the cyan-shaded area presents an unstable system.

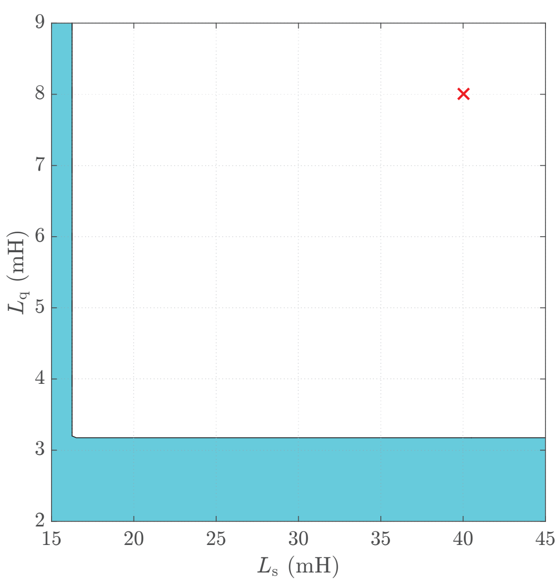


Fig. 5. Stability regions, when the inductances $L_q$ and $L_s$ of the plant model (16) are varied. The white area represents a stable system, whilst the cyan-shaded area represents an unstable system. Inductance estimates of $\hat{L}_s = 40$ mH and $\hat{L}_q = 8$ mH are used in the flux-linkage controller (cf. the red cross).

leads to a stable closed-loop system and it will be used later on in this paper.

As can be seen from (3) and is shown in [18], $L_q$, $L_s$, and $M'_d$ vary during the system operation. However, as can be seen from (2), the variation in $M'_d$ has effect only with eccentric rotors. The effect of variations in the plant-model inductances $L_q$ and $L_s$ is studied here with a centric rotor at the rotor speed of 1500 r/min. The inductance $L_s$ is varied between $15 \ldots 45$ mH and the inductance $L_q$ is varied between $2 \ldots 9$ mH. Fig. 5 shows the stability regions, when the inductance estimates of $\hat{L}_s = 40$ mH and $\hat{L}_q = 8$ mH are used in the flux-linkage controller (cf. the red cross in Fig. 5). The white region represents stable parameter combinations and the cyan-shaded region represents unstable parameter combinations. It can be seen that the closed-loop system remains mostly stable in this parameter region. However, an unstable region appears at the lowest inductance values. If the inductance estimates of $\hat{L}_s = 20$ mH and $\hat{L}_q = 3$ mH would be used in the flux-linkage controller, then the whole parameter space would remain stable. Thus, it is advisable to underestimate rather than overestimate the inductances in the controller.

Next, the effect of the rotor eccentricity is analyzed. Accurate inductance and resistance estimates are assumed and the rotor speed is 1500 r/min. The displacements are varied between $-500 \ldots 500$ $\mu$m both in $x$ and $y$ directions. Fig. 6 shows the stability regions, when the mutual coupling is modeled according to (6) in the plant model (16), but neglected in the flux-linkage controller (i.e., $\hat{\boldsymbol{M}}' = \boldsymbol{0}$). The white region represents stable parameter combinations and the cyan-shaded region represents unstable parameter combinations. It can be seen that the closed-loop system remains stable, when the eccentricity is less than around 350 $\mu$m. If the mutual coupling would be taken into account in the controller, i.e., $\hat{\boldsymbol{M}}' = \boldsymbol{M}'$, then the whole parameter space would remain stable.

## V. Time-Domain Simulations

In this section, the proposed flux-linkage control algorithm is evaluated by means of time-domain simulations. The bandwidth of the flux-linkage control loop is $\alpha_c = 2\pi \cdot 600$ rad/s and the switching frequency is $f_{sw} = 8$ kHz.

### A. Experimental System Under Construction

An experimental setup, including the prototype BSyRM analyzed in this paper, is currently being assembled. Both ends of the BSyRM are supported with commercial active-magnetic-bearings (AMBs) and the shaft of motor can be rotated with an external loading machine. Thus, the torque and the radial-force production capabilities of the prototype BSyRM can be evaluated individually, without a need to operate the BSyRM neither in the speed-control mode nor in the levitation-control mode. The two windings of the BSyRM will be supplied by two separate PWM-operated frequency converters. The gate signals for the converters will be generated from (7) by using OPAL-RT OP5600 fast prototyping platform, where also the proposed flux-linkage control algorithm will be run in real-time. Furthermore, all six phase currents together with the DC-link voltages will be measured and fed back to OP5600 in order to obtain the necessary feedback information for the flux-linkage controller.

The plant model in the simulations is based on the designed prototype BSyRM. The motor is designed using the FEA and the design considerations and the modeling of the motor are reported, e.g., in [18], [19]. The plant model consists of the voltage equations (1), which are integrated in the continuous-time domain to obtain the flux linkages of both windings. Then, static mappings between the flux linkages and each current component are formed based on the FEA results as a form of four-dimensional look-up-tables (4D-LUTs). Four 4D-LUTs are required to obtain all the current components from the flux linkages. Furthermore, two additional 4D-LUTs are formed, based on the FEA results, to map the resulting current components with the radial-force components. The maximum main-winding current amplitude is 45.9 A (peak-to-peak) and the maximum suspension-winding current amplitude is 3.18 A (peak-to-peak). Based on the FEA results, the maximum torque of the motor is 29 Nm and the maximum amplitude of the radial force is 2000 N. The nominal speed of the motor is 1500 r/min. The airgap length of the designed prototype motor is 1 mm.

### B. Results

Two simulation sequences were selected keeping in mind the experimental system, which will be available in the future for experimental verification. The first simulation sequence evaluates the proposed control system, when the LUT-based plant model is used. In the first simulation sequence, the rotor is kept centric with the additional AMBs and rotated 1500 r/min with the external loading machine:

1) The main-winding d-axis current reference $i_{\mathrm{md,ref}}$ is stepped from 0 to 20 A @ 0.01 second
2) The y-axis radial-force reference $F_{\mathrm{y,ref}}$ is stepped from 0 to 300 N @ 0.02 second
3) The torque reference $T_{\mathrm{M,ref}}$ is stepped from 0 to 20 Nm @ 0.03 second and back to 0 Nm @ 0.05 second
4) The x-axis radial-force reference $F_{\mathrm{x,ref}}$ is stepped from 0 to -200 N @ 0.04 second

Fig. 7 shows the results, when the control system is based on the constant magnetic-model parameters. Fig. 7(a) shows the motor torque together with the corresponding main-winding flux-linkage components in rotating coordinates and the main-winding current components in stationary coordinates. Fig. 7(b) shows the radial-force components together with the corresponding suspension-winding flux-linkage components in rotating coordinates and the suspension-winding current components in stationary coordinates.

Fig. 8 shows the results, when the control system is based on the magnetic-model (3). Fig. 8(a) shows the motor torque together with the corresponding main-winding flux-linkage components in rotating coordinates and the main-winding components in stationary coordinates. Fig. 8(b) shows the radial-force components together with the corresponding suspension-winding flux-linkage components in rotating coordinates and the suspension-winding current components in stationary coordinates.

By comparing Figs. 7 and 8, it can be seen that the accuracies of both the torque-control loop and the radial-force control loop are clearly improved, when the control system is based on the explicit-function magnetic model instead of constant parameters. However, the dynamic performances of both the control loops are satisfactory even, if the control system is only based on the constant parameters. Furthermore, it can be seen that the control loop remains clearly stable, even though the plant parameters are varying during the operation. This agrees well with the stability analysis in Fig. 5.

The second simulation sequence evaluates the effect of the rotor eccentricity at the rotor speed of 1500 r/min. Thus, a constant-parameter plant model is used in this simulation and accurate parameter estimates are assumed in the flux-linkage controller. The BSyRM is operated in no-load condition (i.e., $T_{\mathrm{M}} = 0$ Nm) with constant main-winding d-axis current $i_{\mathrm{md}} = 20$ A. Furthermore, a constant radial force of $F_{\mathrm{y}} = 300$ N is produced in $y$ direction. Between the time instants 0.005 s and 0.105 s, the rotor is displaced from $y = 0$ to $y = -400$ $\mu$m in $y$ direction by using the external AMBs.

Fig. 9(b) shows the result, when the mutual coupling is modeled according to (6) both in the plant model (16) and in the flux-linkage controller, i.e., when $\hat{\boldsymbol{M}}' = \boldsymbol{M}'$. Fig. 9(a) shows the result, when the eccentricity is neglected in the controller, i.e., when $\hat{\boldsymbol{M}}' = \mathbf{0}$. It can be seen that the stability of the flux-linkage control loop is lost suddenly and aggressively at 0.1 seconds, when the eccentricity is not compensated for in the controller. The closed-loop system remains stable, when the eccentricity is compensated for in the controller. This result agrees well with the stability analysis in Fig. 6.

## VI. Conclusions

A systematic design method for a state-space flux-linkage control of a dual three-phase-winding BSyRM is proposed in this paper. The design rules for the state-space controller (including state feedback, integral action, and feedforward gains) are obtained using model-based pole-placement methods in the continuous-time domain. The proposed method is easy to apply: the desired closed-loop bandwidth together with an estimated magnetic-model of the motor are required. Furthermore, the proposed method automatically takes into account the mutual coupling between the two windings. Based on the simulation results and eigenvalue analysis, the proposed

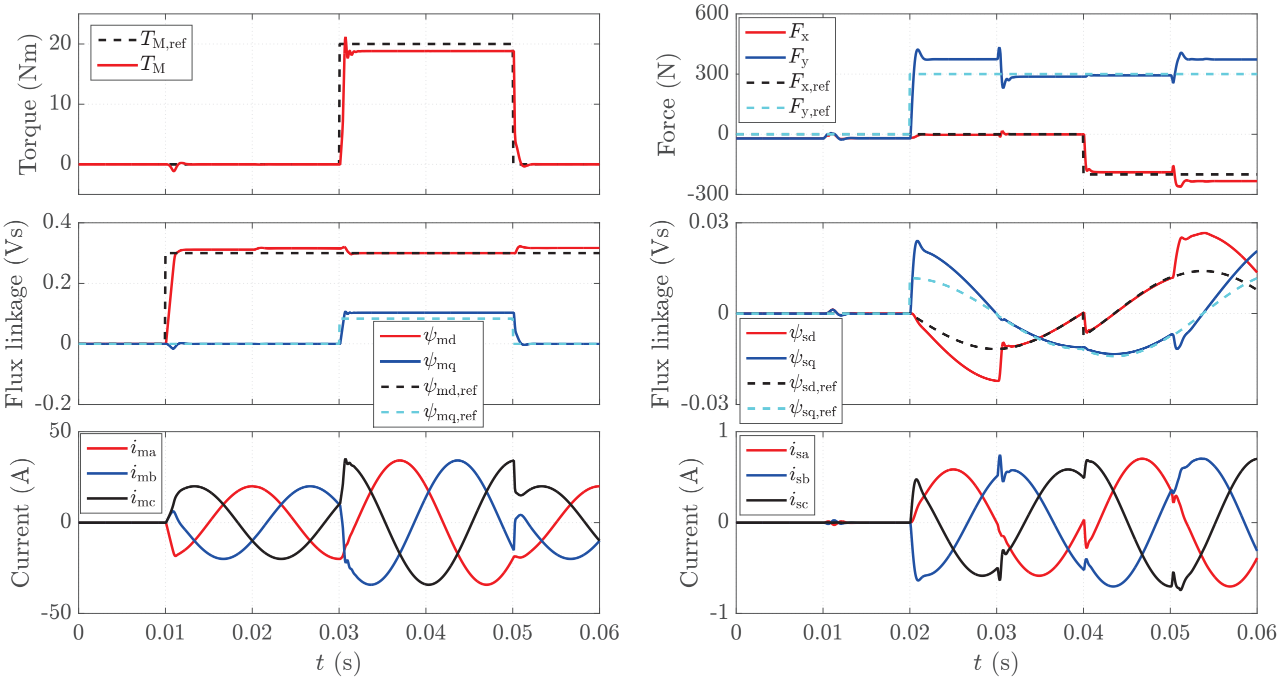


(a) (b)

Fig. 7. Simulation result, when the proposed flux-linkage controller is based on the constant magnetic-model parameters: (a) torque $T_M$ of the motor (the first subplot), together with the main-winding flux linkages $\boldsymbol{\psi}_m$ (the second subplot) and the corresponding main-winding phase currents (the third subplot); (b) radial force $\boldsymbol{F}^s$ of the motor (the first subplot), together with the suspension-winding flux linkages $\boldsymbol{\psi}_s$ (the second subplot) and the corresponding suspension-winding phase currents (the third subplot).

method guarantees robust feedback-loop operation as well as rapid and accurate torque and radial-force production.

## Acknowledgement

The authors gratefully acknowledge The Academy of Finland for the financial support.

## References


[1] H. Mitterhofer, W. Gruber, and W. Amrhein, "On the high speed capacity of bearingless drives," *IEEE Trans. Ind. Electr.*, vol. 61, no. 6, pp. 3119–3126, June 2014.

[2] A. Chiba, T. Deido, T. Fukao, and M. A. Rahman, "An analysis of bearingless ac motors," *IEEE Trans. Energy Convers.*, vol. 9, no. 1, pp. 61–68, Mar. 1994.

[3] W. Gruber, W. Amrhein, and M. Haslmayr, "Bearingless segment motor with five stator elements: Design and optimization," *IEEE Trans. Ind. Appl.*, vol. 45, no. 4, pp. 1301–1308, July/Aug. 2009.

[4] T. Nussbaumer, P. Karutz, F. Zurcher, and J. W. Kolar, "Magnetically levitated slice motors – an overview," *IEEE Trans. Ind. Appl.*, vol. 47, no. 2, pp. 754–766, Mar./Apr. 2011.

[5] J. Asama, Y. Hamasaki, T. Oiwa, and A. Chiba, "Proposal and analysis of a novel single-drive bearingless motor," *IEEE Trans. Ind. Electr.*, vol. 60, no. 1, pp. 129–138, Jan. 2013.

[6] G. L. Kruger, G. van Schoor, and P. A. van Vuuren, "Control of magnetically suspended rotor combined with motor drive system," in *Proc. IFAC'14*, Cape Town, South Africa, Aug. 2014, pp. 7252–7257.

[7] K. C. Lee, Y. H. Jeong, D. H. Koo, and H. J. Ahn, "Development of a radial active magnetic bearing for high speed turbo-machinery motors," in *Proc. IEEE SICE-ICASE'06*, Busan, South Korea, Oct 2006, pp. 1543–1548.

[8] R. P. Jastrzebski, "Signal-based $H_\infty$ optimal control for AMB system based on genetic algorithm," in *Proc. IEEE ICCA'09*, Christchurch, New Zealand, Dec. 2009, pp. 715–721.

[9] A. Smirnov, R. P. Jastrzebski, K. Hynynen, and O. Pyrhönen, "Comparison of suboptimal control methods in magnetic levitation system," in *Proc. IEEE EPE'13*, Lille, France, Sept 2013.

[10] C. Michioka, T. Sakamoto, O. Ichikawa, A. Chiba, and T. Fukao, "A decoupling control method of reluctance-type bearingless motors considering magnetic saturation," *IEEE Trans. Ind. Appl.*, vol. 32, no. 5, pp. 1204–1210, Sep./Oct. 1996.

[11] L. Harnefors and H.-P. Nee, "Model-based current control of ac machines using the internal model control method," *IEEE Trans. Ind. Appl.*, vol. 34, no. 1, pp. 133–141, Jan./Feb. 1998.

[12] F. Briz, M. W. Degner, and R. D. Lorenz, "Dynamic analysis of current regulators for AC motors using complex vectors," *IEEE Trans. Ind. Appl.*, vol. 35, no. 6, pp. 1424–1432, Nov./Dec. 1999.

[13] M. Hinkkanen, H. A. A. Awan, Z. Qu, T. Tuovinen, and F. Briz, "Current control for synchronous motor drives: Direct discrete-time pole-placement design," *IEEE Trans. Ind. Appl.*, vol. 52, no. 2, pp. 1530–1541, Mar./Apr. 2016.

[14] Z. Xu, D.-H. Lee, and J.-W. Ahn, "Modeling and control of a bearingless switched reluctance motor with separated torque and suspending force poles," in *Proc. IEEE ISIE'13*, Taipei, Taiwan, May 2013.

[15] H. Zhu, Q. Cheng, and C. Wang, "Modeling of bearingless permanent magnet synchronous motor based on mechanical to electrical coordinates transformation," *Sci. China Ser. E, Technol. Sci.,*, vol. 52, no. 12, p. 3736 3744, Dec. 2009.

[16] K. Hijikata, N. Ando, M. Takemoto, and S. Ogasawara, "A decoupling method for current regulation in bearingless motors using ac suspension current," in *Proc. ICEMS'14*, Hangzhou, China, Oct 2014, pp. 2310–2314.

[17] S. Yamamoto, T. Ara, and K. Matsuse, "A method to calculate transient characteristics of synchronous reluctance motors considering iron loss and cross-magnetic saturation," *IEEE Trans. Ind. Appl.*, vol. 43, no. 1, pp. 47–56, Jan./Feb. 2007.

[18] S. E. Saarakkala, M. Sokolov, V. Mukherjee, J. Pippuri, K. Tammi, A. Belahcen, and M. Hinkkanen, "Flux-linkage model including cross-saturation for a bearingless synchronous reluctance motor," in *Proc. ISMB15*, Kitakyushu, Japan, Aug. 2016.

[19] V. Mukherjee, J. Pippuri, A. Belahcen, S. E. Saarakkala, M. Hinkkanen, and K. Tammi, "Finite element analysis for bearingless operation of a multi flux barrier synchronous reluctance motor," in *Proc. ICEMS'15*, Pattaya, Thailand, Oct. 2015.

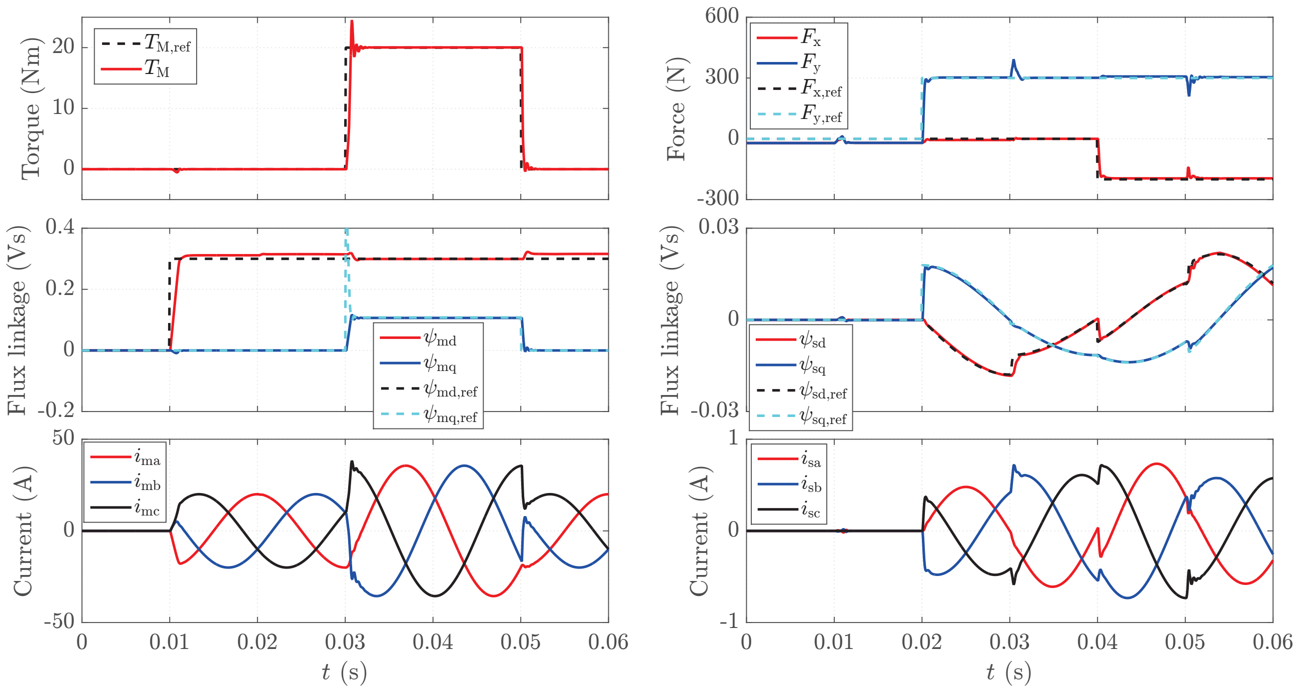


(a) (b)

Fig. 8. Simulation result, when the proposed flux-linkage controller is based on the magnetic-model (3): (a) torque $T_M$ of the motor (the first subplot), together with the main-winding flux linkages $\boldsymbol{\psi}_m$ (the second subplot) and the corresponding main-winding phase currents (the third subplot); (b) radial force $\boldsymbol{F}^s$ of the motor (the first subplot), together with the suspension-winding flux linkages $\boldsymbol{\psi}_s$ (the second subplot) and the corresponding suspension-winding phase currents (the third subplot).

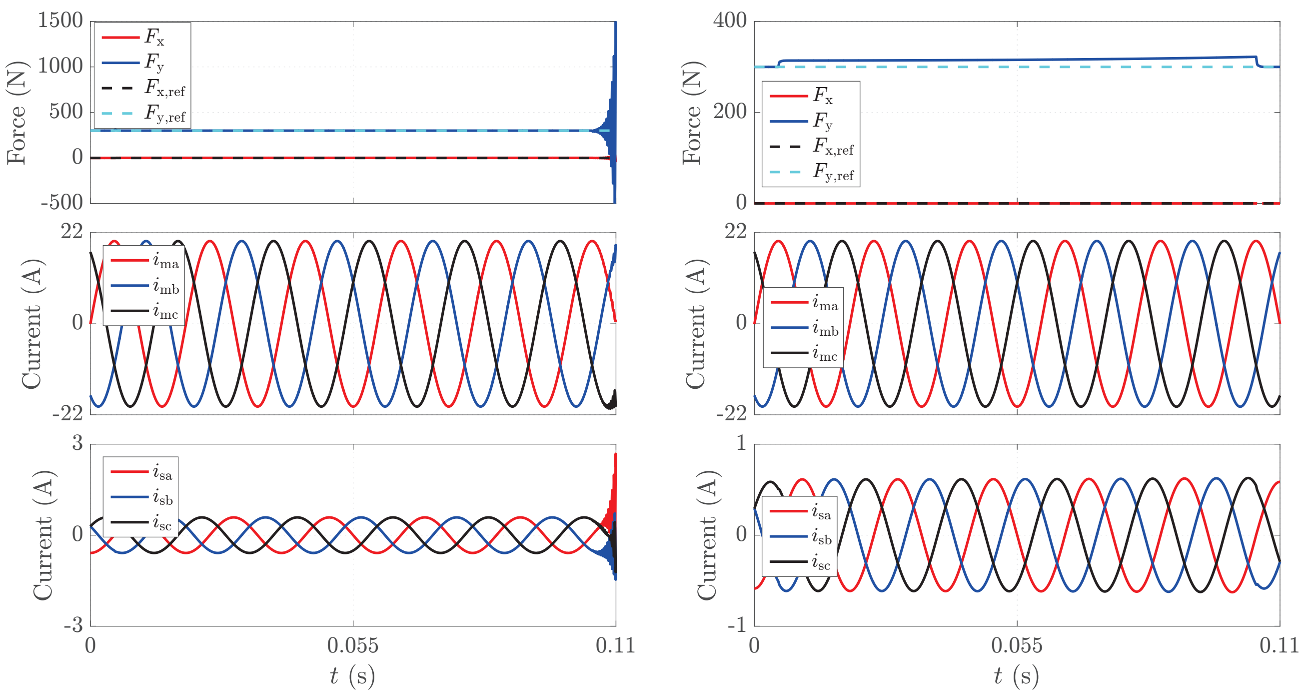


(a) (b)

Fig. 9. Simulation result, when the rotor of the BSyRM is displaced from $y = 0$ to $y = -400$ $\mu$m between the time instants 0.005 s and 0.105 s. Radial forces $\boldsymbol{F}^s$ of the motor (the first subplots), together with the main-winding phase currents (the second subplots) and the suspension-winding phase currents (the third subplots), when the mutual coupling (6) is: (a) neglected in the controller; and (b) taken into account in the controller.